Circ J
doi:10.1253/circj.CJ-17-0381

ORIGINAL ARTICLE
Cardiovascular Surgery

Analysis of Computational Fluid Dynamics and Particle Image Velocimetry Models of Distal-End Side-to-Side and End-to-Side Anastomoses for Coronary Artery Bypass Grafting in a Pulsatile Flow

Yoshiko Shintani, MD; Kenji Iino, PhD; Yoshitaka Yamamoto, PhD; Hiroki Kato, PhD; Hirofumi Takemura, PhD; Takahiro Kiwata, PhD

Background: Intimal hyperplasia (IH) is a major cause of graft failure. Hemodynamic factors such as stagnation and disturbed blood flow are involved in IH formation. The aim of this study is to perform a comparative analysis of distal-end side-to-side (deSTS) and end-to-side (ETS) anastomoses using computational fluid dynamics (CFD) after validating the results via particle image velocimetry (PIV).

Methods and Results: We investigated the characteristics of our target flow fields using CFD under steady and pulsatile flows. CFD via PIV under steady flow in a 10-times-actual-size model was validated. The CFD analysis revealed a recirculation zone in the heel region in the deSTS and ETS anastomoses and at the distal end of the graft, and just distal to the toe of the host artery in the deSTS anastomoses. The recirculation zone sizes changed with the phase shift. We found regions of low wall shear stress and high oscillating shear index in the same areas. The PIV and CFD results were similar.

Conclusions: It was demonstrated that the hemodynamic characteristics of CFD and PIV is the difference between the deSTS and ETS anastomoses; that is, the deSTS flow peripheral to the distal end of the graft, at the distal end and just distal to the toe of the host artery is involved in the IH formation.

Key Words: Computational fluid dynamics; Coronary artery bypass grafting; Distal-end side-to-side anastomosis; Intimal hyperplasia; Particle image velocimetry

Coronary artery bypass grafting (CABG) has long been used to facilitate arterial revascularization. Anastomotic intimal hyperplasia (IH) is a major cause of graft failure. It has been shown that hemodynamic factors are involved in IH formation and progression.[1,2] These factors include disturbed blood flow patterns, low and oscillating wall shear stress (WSS), sufficiently high WSS, large spatial WSS gradients, and the stagnation of blood cells.[3,4]

Grafts to the coronary artery commonly involve end-to-side (ETS) anastomoses. It has been shown that, after such procedures, IH develops predominantly at the toe and heel of such anastomoses and on the arterial floor across the junction, where the disturbance of flow patterns and other hemodynamic factors have reportedly been observed.[2,5]

Meanwhile, several recent studies have reported the usefulness of distal-end side-to-side (deSTS) anastomoses.[6,7] Umezu et al[8] reported that deSTS anastomoses lose less energy than ETS anastomoses. However, a detailed 3-dimensional assessment of the hemodynamic characteristics of deSTS anastomosis has not yet been reported. This study is designed to investigate flow fields in deSTS-simulated left internal thoracic artery (LITA)-left anterior descending artery (LAD) anastomoses, examine differences between deSTS and ETS anastomoses in flow fields using computational fluid dynamics (CFD), and validate the findings via particle image velocimetry (PIV).

Methods

The internal thoracic artery (ITA) is a proven excellent conduit to use when performing CABG. ETS or deSTS anastomoses are usually used to connect the distal end of the ITA-LAD anastomoses. Therefore, in our model, it was assumed that the anastomoses were to the distal end of the LITA-LAD anastomoses.

A series of separate studies were performed. First, steady and pulsatile flows were investigated in an actual size model (Model A) using CFD. Next, CFD simulations and PIV measurements of the steady flow were used to validate

Received April 11, 2017; revised manuscript received July 2, 2017; accepted July 4, 2017; released online August 19, 2017 Time for primary review: 48 days

Department of Thoracic, Cardiovascular and General Surgery (Y.S., K.I., Y.Y., H.K., H.T.), School of Mechanical Engineering (T.K.), Kanazawa University, Kanazawa, Japan

Mailing address: Yoshiko Shintani, MD, Department of Thoracic, Cardiovascular and General Surgery, Kanazawa University, 13-1 Takara-machi, Kanazawa 920-8641, Japan. E-mail: Y.Shintani@med.kanazawa-u.ac.jp

ISSN-1346-9843

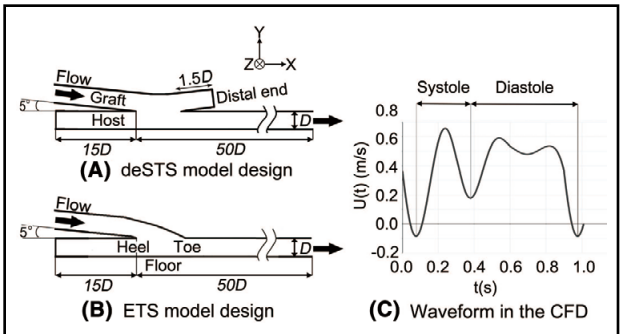

Figure 1. Configuration of the bypass (**A**) distal-end side-to-side (deSTS) model design and (**B**) end-to-side (ETS) model design and (**C**) the pulsatile blood-flow waveform used in the computational fluid dynamics (CFD) simulation.

the findings in a model that was 10 times the actual size (Models B and C).

Numerical Simulations

Figure 1A,B show the coronary artery geometry of the deSTS and ETS models. In Model A, the graft and host arteries were assumed to be circular conduits of diameter D=2.0 mm with inlet and outlet angles of 5°; these values being typical for LITA-LAD anastomoses. The graft and host arteries extended distally and proximally by 50 D (=100 mm) and 15 D (=30.0 mm), respectively, from the heel of the anastomosis. In the deSTS model, the distal end of the graft was 1.5 D (=3.0 mm) long. The anastomosis site was designed to make the areas of the anastomoses nearly identical.

Model B, which was 10 times the size of Model A, was designed to validate the experimental data via PIV and to investigate the effects of scale. The graft and host arteries were assumed to be D=20.0 mm and, in the deSTS model, the distal end of the graft was 1.5 D (=30.0 mm) long.

It was assumed that the blood flow was 3-dimensional, time-dependent, incompressible, isothermal, Newtonian, homogeneous, and laminar. The governing equations were as follows.

The continuity equation:

$$\nabla \cdot v=0$$

The Navier-Stokes equation:

$$\rho \frac{dv}{dt}+\rho(v \cdot \nabla)v=-\nabla p+\mu\nabla^2 v,$$

where v is the velocity vector, t is time, p is pressure, ρ is the density, and μ is the dynamic viscosity.

In Model A, blood was assumed to have a density (ρ) of 1.06×10^3 kg m^{-3} and a viscosity (μ) of 4.00×10^{-3} kg m^{-1} s^{-1}. In addition, to meet the conditions of the working fluid used in the validation experiment, in Model B, blood was assumed to have a density of 1.69×10^3 kg m^{-3} and a viscosity of 2.00×10^{-1} kg m^{-1} s^{-1}. The vessel walls were assumed to be rigid and impermeable, the gravitational force was assumed to be negligible, and vessel walls were assumed to have no-slip characteristics. The outflow boundary conditions corresponded to a traction-free surface. The outlet boundary conditions were placed 50 D downstream from the anastomosis to avoid perturbations in the upstream flow field. We used the outlet pressure as the outflow boundary condition. The gauge pressure of the outlet pressure was 0 Pa.

Using a commercial CFD software program, ANSYS Fluent 15.0 (ANSYS Japan, Tokyo, Japan), the finite volume method was used to solve the continuity and Navier-Stokes equations. The numerical domain was meshed using tetrahedral unstructured grids. For the deSTS version of Model A, the number of nodes was set to approximately 4.60×10^5 and the minimum length to 1.91×10^{-5} mm, whereas for the ETS version of Model A, the number of nodes was set to approximately 4.80×10^5 and the minimum length of nodes to 1.26×10^{-5} mm. For the deSTS version of Model B, the number of nodes was set to approximately 9.10×10^5 and the minimum length to 1.06×10^{-4} mm, whereas for the ETS version of Model B, the number of nodes was set to approximately 8.90×10^5 and minimum length of nodes to 1.35×10^{-4} mm. The mesh sensitivity was tested for the velocity and WSS by varying the number of grid cells.

We assumed that the proximal host artery was fully occluded. The inlet Reynolds number ($\mathrm{Re}=\rho U[\mathrm{t}]\,D/\mu$) was 5.14 ($U$[t]=$9.70\times10^{-3}$ m/s for Model A and U[t]=3.31×10^{-2} m/s for Model B, where U[t] is the inlet velocity) in the steady flow. For pulsatile flow, the flow waveform and velocity profile were based on measured by magnetic resonance phase velocity mapping within a CABG.[9] However, as shown in **Figure 1**, for this study, some modifications were made to smooth the waveform, including the adoption of a time period of 0.90s. Assuming a normal physiological resting heart rate (f) of 66 beats/min, the waveform was scaled to have a Womersley unsteadiness parameter [$\alpha=(D/2)\cdot(2\pi f\rho/\mu)^{0.5}$] of 1.35 and a mean Reynolds number of 212. The time step was set to be sufficiently fine ($<10^{-5}$) to achieve a sufficiently low Courant number, and transient calculations for 2 cardiac cycles were performed. The iterations were considered to have converged when both the residuals for any velocity component of the momentum equations and the mass creation rate for the continuity equations had consistently dropped to 5.00×10^{-5} within each time step.

Particle Image Velocimetry Measurement

Model C was made of ultraviolet curable resin (Objet Veroclear RGD810; Stratasys, Eden Prairie, MN, USA) and produced using a 3-dimensional printer. It was a hollowed-out square box of the same shape and dimensions as the 10-times-actual-size model (Model B). A mixture of 46.2% glycerin, 49.5% sodium iodide (NaI), and 4.30% water by volume was used as the working fluid in this study. The density and viscosity of this Newtonian mixture were 1.69×10^3 kg m^{-3} and 2.00×10^{-1} kg m^{-1} s^{-1}, respectively, at a working temperature of 25.0°C. The mixture was formulated to match the refractive index of the model. Silver-coated hollow glass spheres with a mean size of 10.0 μm and a density of 1.40 g cm^{-3} (S-HGS-10; Dantec Dynamics, Skovlunde, Denmark) were used as seeding particles. Each resin model was incorporated into a flow circuit, and a gear pump system (2NL10, Heishin Mohno pump; Heishin, Kobe, Japan) was used to generate the inlet flow waveform. The flow rate was measured and monitored with a transit-time volume flowmeter (Butterfly Flowmeter BF2004; Medi-stim, Oslo, Norway) immediately downstream of the test section. The flow rate was Q=620 mL/min, and the Reynolds number was calculated to be 5.14.

The PIV system consisted of a 15-Hz dual-head pulsed Nd:YAG laser (NANO L200-15PIV; Litron Lasers, Rugby, Warwickshire, UK) and a CCD camera (Flowsense EO

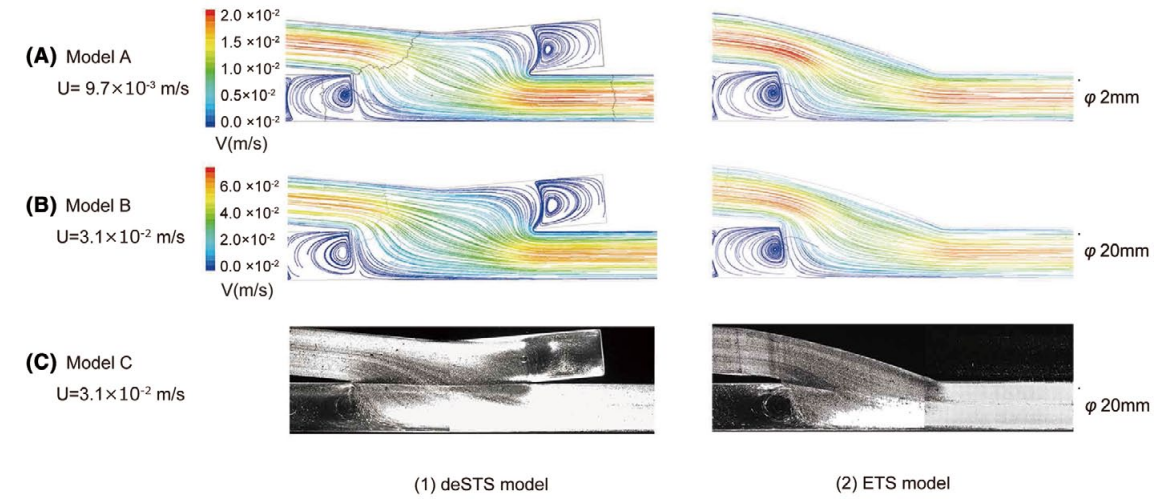

Figure 2. Streamlines in the X–Y symmetry plane of numerical simulations with Models (**A**) A and (**B**) B and (**C**) superimposing images (200 images) of particle image velocity (PIV) measurements of Model C in (**1**) the deSTS model and (**2**) the ETS model at Re=5.14. $V=\sqrt{u^2+v^2+w^2}$. u, v, w, the velocity vector component of the X, Y, Z coordinates.

5M; Dantec Dynamics). Two images of 1,600×1,200 pixels with a time interval of approximately 0.10–1.20 ms, depending on the velocity magnitude, were recorded in rapid succession. These recordings were analyzed using a cross-correlation method with interrogation areas of 32×32 pixels overlapping by 50% on each of their sides. For each time step, 200 valid recordings were used to provide an averaged vector field.

Hemodynamic Parameters

The velocity profile (streamlines and velocity vectors), distribution of WSS, oscillating shear index (OSI), and time-average WSS (TAWSS) were assessed; these variables were calculated as follows:

$$\text{WSS: } \overrightarrow{\tau w} = \mu \frac{dW}{dl},$$

where l is the distance to the wall, W is the velocity vector component parallel to the wall, and μ is the viscosity.

OSI was originally proposed by Ku et al[10] as a means of quantifying the oscillatory nature of the WSS, and is calculated as follows:

$$\text{OSI}= \frac{1}{2}\left(1.0 - \frac{\left|\int_0^T \overrightarrow{\tau w}\, dt\right|}{\int_0^T \left|\overrightarrow{\tau w}\right| dt}\right),$$

where T is the time for one cardiac cycle.

OSI values range from 0 to 0.5, 0 indicating only one direction of WSS and 0.5 indicating completely unsteady WSS. Areas with high-OSI values are predisposed to endothelial dysfunction and plaque progression.

$$\text{TAWSS}=\frac{1}{T}\int_0^T \left|\overrightarrow{\tau w}\right| dt.$$

Results

Analysis and Validation of Steady Flow Using CFD and PIV

The computed streamlines in the X–Y symmetry plane of numerical simulations with Models A and B and the actual streamlines of Model C were visualized by superimposing images (200 images) of PIV measurements of the deSTS and ETS models, as shown in **Figure 2**. In numerical simulations with Model A of both the deSTS and ETS models, CFD showed the presence of a recirculation zone in the heel region, with a stagnation point on the host artery floor where the graft flow impinges on the host artery floor. In addition, the computed streamlines of the deSTS models showed an expansion of the graft flow at the anastomosis site, with some of the flow subsequently turning into the host artery from the ceiling of the graft in the distal part of the anastomosis, and the remainder of the flow flowing into the distal end of the graft and generating a recirculation zone. The pattern of the computed streamlines of Model B was similar to that of Model A. Moreover, the actual streamlines of Model C revealed a pattern similar to the computed streamlines in both the deSTS and ETS anastomoses in Model B.

As shown in **Figure 3**, velocity profiles at the center of the anastomosis and toe region and 1 D from the toe of the anastomosis were analyzed using CFD in Models A and B and via PIV using Model C with the deSTS and ETS models in steady flow. The maximum velocity magnitude [V_{max} (t)] at the center of the anastomosis in Models A, B, and C was 0.95 at Y_{floor}/D=1.21, 0.94 at Y_{floor}/D=1.25, and 0.91 at Y_{floor}/D=1.00 of deSTS models, and 1.24 at Y_{floor}/D=0.92, 1.22 at Y_{floor}/D=0.93, and 1.25 at Y_{floor}/D=0.93 of ETS models, respectively (**Figure 3A**). The velocity profiles from CFD and PIV demonstrate that the maximum velocity magnitude at the center of the anastomosis is less in deSTS models than in ETS models. The V_{max} (t) at the toe region in Models A, B, and C was 1.92 at Y_{floor}/D=0.53, 1.91 at Y_{floor}/D=0.51, and 1.94 at Y_{floor}/D=0.49 of deSTS models,

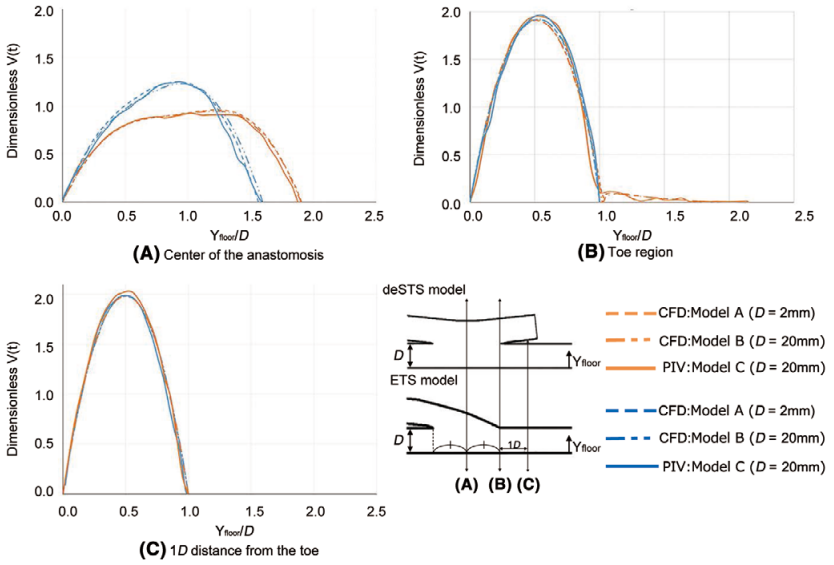

Figure 3. Comparison of the velocity profiles in the X–Y symmetry plane (**A**) at the center of the anastomosis; (**B**) at the toe region; and (**C**) at a distance 1 *D* from the toe after numerical simulations with Models A and B, and experimental measurements with Model C. Y_{floor}/D, distance from the floor.

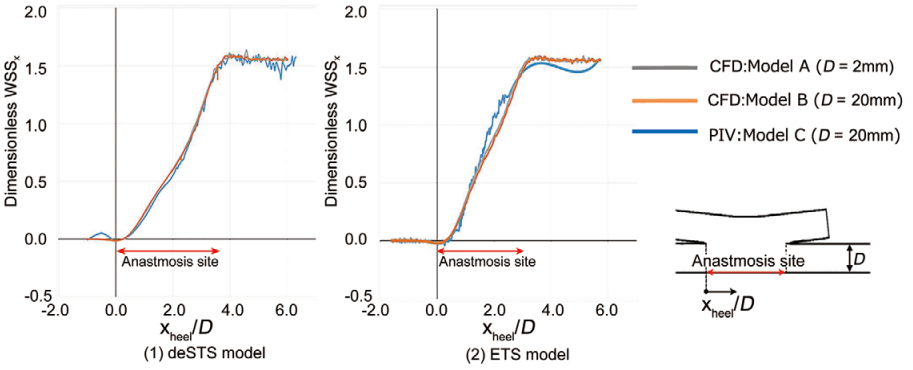

Figure 4. Comparisons of dimensionless WSS_x variations in the X–Y symmetry plane on the host artery floor after numerical simulations with Models A and B, and experimental measurements with Model C in (**1**) the deSTS model and (**2**) the ETS model. WSS, wall sheer stress; X_{heel}/D, distance from the heel.

and 1.92 at Y_{floor}/D=0.53, 1.92 at Y_{floor}/D=0.52, and 1.96 at Y_{floor}/D=0.55 of ETS models, respectively (**Figure 3B**). The V_{max} (t) at 1 *D* distance from the toe in Models A, B, and C was 1.98 at Y_{floor}/D=0.50, 1.98 at Y_{floor}/D=0.50, and 2.03 at Y_{floor}/D=0.51 of deSTS models, and 1.98 at Y_{floor}/D=0.51, 1.98 at Y_{floor}/D=0.51, and 1.98 at Y_{floor}/D=0.49 of ETS models, respectively (**Figure 3C**). Both CFD and PIV showed the same velocity profile at a distance of 1 *D* from the toe, where it becomes a Poiseuille flow in both deSTS and ETS models.

Variations in the dimensionless X component of WSS (WSS_x) in the X–Y symmetry plane on the host artery floor for numerical simulations of Models A and B and experimental measurements in Model C in the deSTS and ETS models are shown in **Figure 4**. The WSSx of Models A, B, and C in deSTS model were 0.60, 0.60, and 0.56 at X_{heel}/D=2.0, and 1.58, 1.58, and 1.56 at X_{heel}/D=4.0, respectively (**Figure 4-(1)**). The WSSx of Models A, B and, C in ETS model were 0.91, 0.85, and 1.07 at X_{heel}/D=2.0, and 1.57, 1.55, and 1.51 at X_{heel}/D=4.0, respectively (**Figure 4-(2)**). These results show good qualitative agreement between CFD simulations and PIV measurements in deSTS and ETS models for both the velocity profiles and the distributions of WSS_x.

Analysis in a Pulsatile Flow Using CFD in Model A

The streamlines of the deSTS and ETS models in the X–Y symmetry plane in various phases are shown in **Figure 5-(1)** and **5-(2)**, respectively.

In the deSTS models, there was a recirculation zone at the anastomosis site when the graft flow changed from backward to forward in both models (**Figure 5A**). With the exception of a period of low flow velocity, there was a recirculation zone in the heel region at all other times (**Figure 5B–D**; **Movie S1**). The graft flow expanded at the anastomosis site, with some flow into the distal end of the graft, generating a recirculation zone, whereas the remainder of the flow turned into the host artery from the ceiling

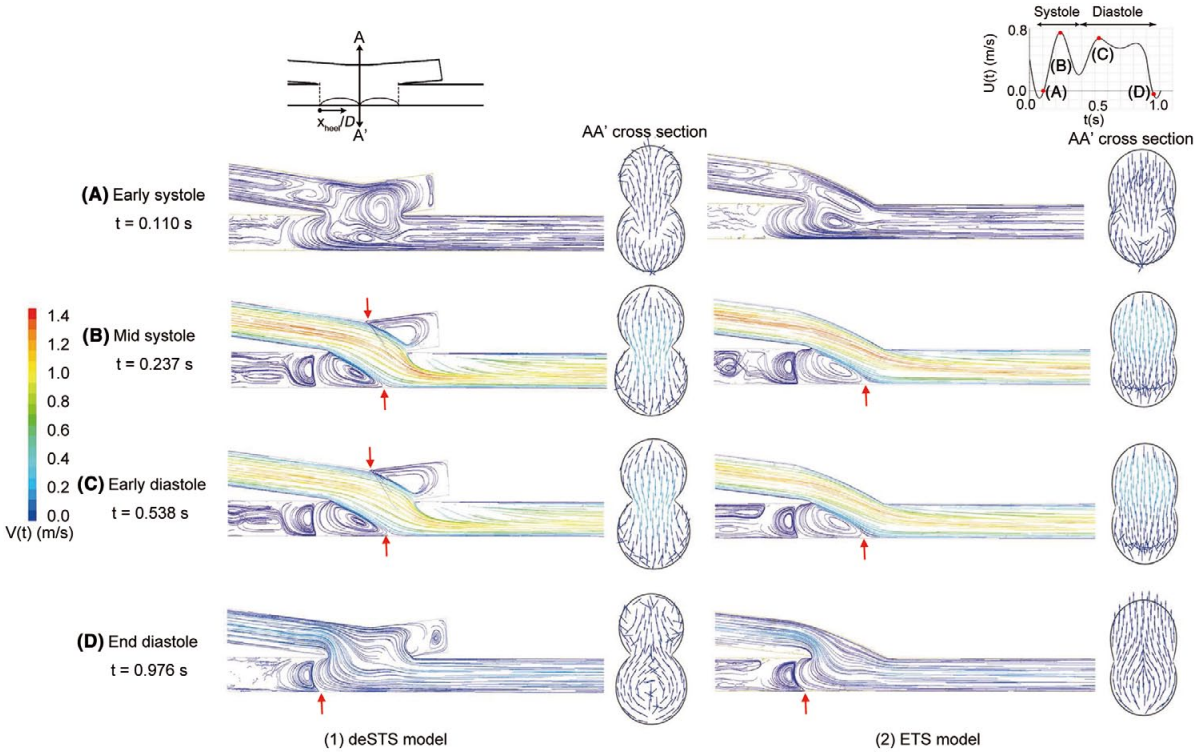

Figure 5. Streamlines in the anastomotic region of (**1**) the deSTS model and (**2**) the ETS model in the following phases: (**A**) early systole: U (t)=0 m/s, (**B**) mid systole: U (t)=0.65 m/s; (**C**) early diastole: U (t)=0.59 m/s; and (**D**) end diastole: U (t)=−0.083 m/s. Arrows represent stagnation points. X_{heel}/D, distance from the heel. U (t), inlet velocity.

of the graft in the distal part of the anastomosis, creating a stagnation point where the graft flow impinged on the host artery floor. Some of the vortex flow in the heel region and the flow impinging on the host artery flowed along the wall and gathered on the roof of the host artery distal to the toe. The flow in the recirculation zone at the distal end met the graft flow, creating a stagnation point at the graft. Thereafter, the flow gathered into the roof of the host artery distal to the toe. The recirculation zone increased in size when the flow velocity increased with the phase shift; therefore, the stagnation point moved during the cardiac cycle. The stagnation point on the X–Y symmetry plane on the host artery floor (**Figure 5** arrows) was moved from −0.94 to 3.99 distance from the heel (X_{heel}/D) in the deSTS model, and from −1.02 to 3.90 (X_{heel}/D) in the ETS model (**Figure 5**; **Movies S1**,**S2**). The main stream shifted to the host artery floor around the toe and was, therefore, sparse downstream from the toe where the recirculation zone formed. Then, the main stream returned to the center downstream (**Figure 5B**,**C**; **Movie S1**). Although the graft flow was backward, there were recirculation zones in the heel region and at the distal end, as shown in **Figure 5D**.

In the ETS models, the same characteristics were observed, namely, recirculation at the anastomosis site (**Figure 5A**) and in the heel region (**Figure 5B**,**C**; **Movie S2**), with a stagnation point where the graft flow impinged on the host artery floor that moved during the cardiac cycle. Meanwhile, it differed from the deSTS models in that the main stream passed near the toe; therefore, it did not form a recirculation zone distal to the toe.

The velocity vectors and isovelocity contours of the deSTS and ETS models at the various cross-sections and phases are shown in **Figure 6-(1)** and **6-(2)**, respectively. The center flow velocity at the center of the anastomosis was found to be less in the deSTS models than in the ETS models for all phases. In the deSTS models, there was reverse flow around the toe when the velocity was >0.11 m/s (**Figure 6B**,**C**). In both the deSTS and ETS models, the direction of the vector at the toe shifted toward the host artery floor (**Figure 6B**,**C**). This tendency was stronger in the deSTS models than in the ETS models because of the reverse flow and the flow turning into the anastomosis site. In both the deSTS and ETS models, the velocity contours were the same at all points beyond 10 *D*. When the graft flow was backward, the main stream shifted toward the ceiling of the graft (**Figure 6D**).

The distributions of TAWSS and the OSI of the deSTS and the ETS models are shown in **Figure 7-(1)** and **7-(2)**, respectively. The maximum WSS was generated in the toe of the deSTS model when the flow velocity peaked (max WSS=163.02 Pa, t=0.237 s). The TAWSS in the distal host artery was the same in both models (**Figure 7A**). There was a low-TAWSS area (<0.5 Pa) in the heel region in both the deSTS and ETS models. In addition, there were low-TAWSS areas at the distal end in the deSTS model (**Figure 7A**).

There were high-OSI areas in the upstream host artery and from the heel to the floor in the deSTS and ETS models, as well as at the distal end of the graft and distal to the

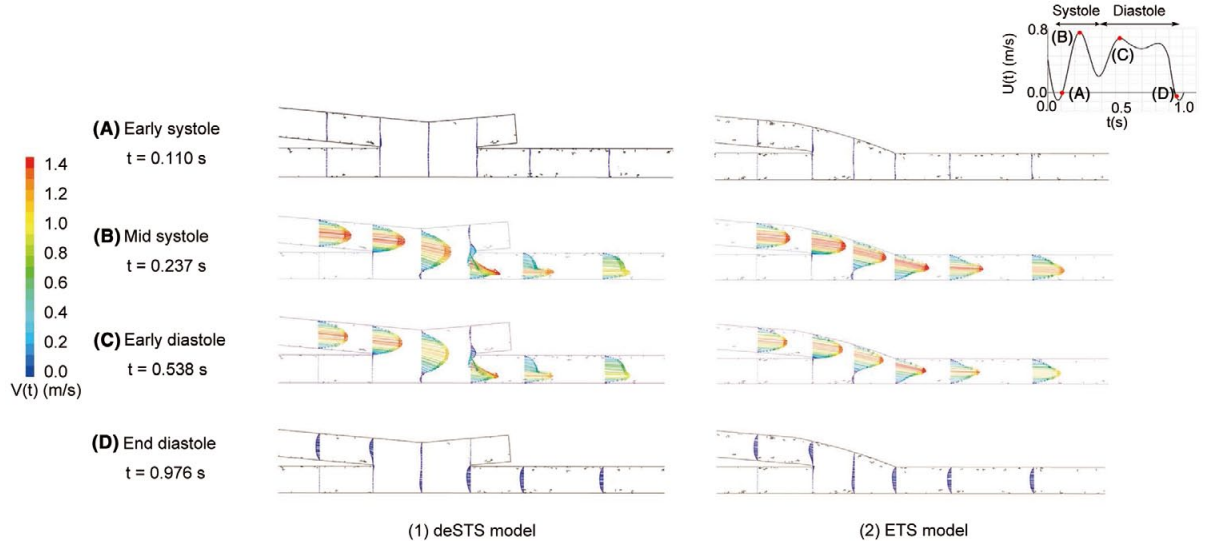

Figure 6. The velocity field in the anastomotic region of (**1**) the deSTS model and (**2**) the ETS model in various phases (X_{heel}/D=−2.0, anastomosis center, X_{toe}/D=0.0, 2.0, 5.0): (**A**) early systole: U (t)=0 m/s: (**B**) mid systole: U (t)=0.65 m/s; (**C**) early diastole: U (t)=0.59 m/s; and (**D**) end diastole: U (t)=−0.083 m/s.

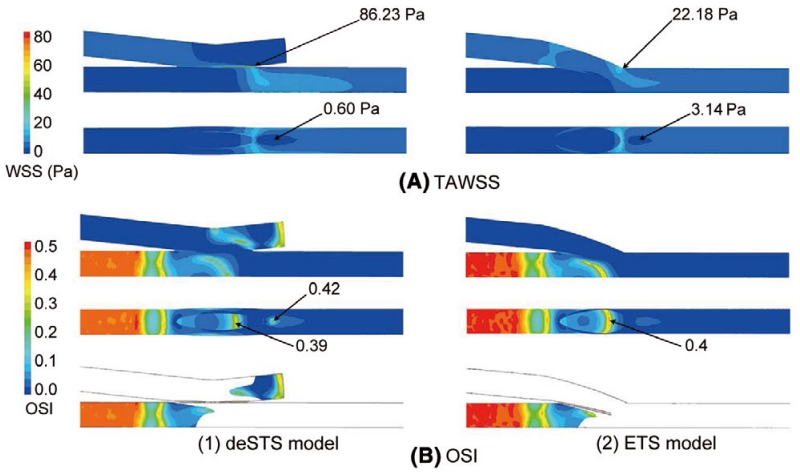

Figure 7. (**A**) Distributions of time-average wall shear stress (TAWSS) in (**1**) the deSTS model and (**2**) the ETS model: (**Upper**) lateral side of an anastomosis site and (**Lower**) anastomosis side of a graft removed from the models. (**B**) Distributions of oscillating shear index (OSI) in both models: (**Upper**) lateral side of an anastomosis region; (**Middle**) anastomosis side of a graft removed from the models; and (**Lower**) extracted low-WSS region (WSS <0.5 Pa).

toe in the deSTS model. Moreover, the high-OSI areas were in locations similar to the stagnation point when the velocity was high. The stagnation point (WSS=0 Pa) in the X–Y symmetry plane moved according to the flow rate (data not shown).

The high-OSI and the low-WSS areas were upstream of the heel and on the sidewall near the heel in both models. In addition, the high-OSI and low-WSS areas were at the distal end and on the sidewall of the graft near the toe in the deSTS model (**Figure 7B**).

Discussion

In this study, the hemodynamics of the deSTS and ETS anastomosis models were both comprehensively studied using numerical simulations and validated via PIV measurements.

In the deSTS model, several low-WSS and high-OSI areas were identified in the heel and the distal end, on the host artery floor and at the graft along the border between the graft flow and recirculation zones, and around the toe. A recirculation zone formed because of the slow flow in the occluded artery in the heel and the distal end, the stagnation point oscillated because of the recirculation zones changed size during the cardiac cycle on the host artery floor and at the graft along the border between the graft flow and recirculation zones, and a vortex formed around the toe by shifted the main stream to the host artery floor, contributing to the development of several low-WSS and high-OSI areas.

Development of anastomotic IH is a major cause of chronic graft failure. A number of studies have proposed various theories concerning the pathophysiology of IH.

When blood flow is steady and unidirectional, intimal cells assume a spindle form; conversely, with oscillating flow, intimal cells remain polygonal in shape, leading to intimal thickening.[11] WSS in human arteries characteristically is on the order of 1–2 Pa.[12] Relatively high WSS or high wall shear rate or low WSS may have adverse effects. High WSS (>38.9 Pa) causes cell degeneration,[13] whereas low WSS (<0.5 Pa)[14] in combination with high OSI promotes IH.[15,16] Moreover, high shear rates cause explosive platelet thrombosis associated with life-threatening hemorrhage or arterial occlusion.[17] Even though attempts have been made to improve the hemodynamic characteristics of coronary artery bypasses,[18] the performance of the resulting configurations remains controversial.

CABGs are generally configured as ETS anastomoses. deSTS anastomoses of the LITA to the target coronary vessel are designed to minimize surgical damage to the LITA. With this technique, proportional suturing is easy and straightforward; the coronary and graft incisions can be perfectly matched via proportional stitching. In addition, in cases of doubt, it is easy to confirm that an anastomosis has been established by reopening the anastomosis via the distal end of the graft, obviating the need to re-suture the anastomosis. Finally, the distal end of the graft can be held beyond the surgical clip with forceps without damaging the arterial graft, making it easier to perform the anastomosis.[7,19,20] Therefore, this technique is often used, especially in Japan. Several studies have reported the hemodynamics of STS anastomoses in sequential bypass grafting.[21,22] However, a detailed 3-dimensional assessment of the hemodynamic characteristics of deSTS anastomoses has not yet been reported.

Several studies[2,3] have reported that, in ETS models, a recirculation zone forms in a low-WSS and high-OSI area in the heel as a result of the interaction between flow from the graft and the relatively slow flow in the occluded proximal artery. There is also a stagnation point on the host artery floor where the graft flow impinges on it. The location of this stagnation point reportedly oscillates during the cardiac cycle, resulting in low-magnitude, high-oscillatory WSS on the host artery floor.[2] In this study, we found that the hemodynamic characteristics of our ETS model are similar (**Figure 5-(2)**; **Movie S2**) to those previously reported.[2,3] Moreover, our findings were very similar to those found from the deSTS model, in which a recirculation zone is created via the interaction of the flow from the graft with the relatively slow flow in the occluded distal end. Therefore, in the deSTS model, there is a low-WSS region at the distal end (**Figure 7-(1)**).

At the distal end, there was low WSS because the relatively slow flow in the occluded distal end created a high-OSI area bordering the recirculation zone (**Figure 7A**). The direction of the recirculation zone depends on the direction of the inlet flow, resulting in a low-OSI area at the distal end. Because the main stream went toward the distal end in the deSTS model, there were also some differences between the deSTS and ETS models in the distribution of the low-WSS area in the heel region (**Figure 7A**). In addition, the high-OSI areas of the floor were larger in the ETS model than in the deSTS model (**Figure 7B**). This occurred because the main stream of the deSTS model shifted to the floor, resulting in the stagnation point moving more widely and TAWSS being higher on the floor in the deSTS model than in the ETS model (**Movies S1**,**S2**). We found a small recirculation zone downstream of the anastomosis that resulted in high OSI and relative low WSS (OSI=0.42, WSS=0.60 Pa), as shown in **Figure 7-(1)**; this was caused by changes in the size of the recirculation zone with changes in the flow velocity. Even though the WSS was greater than the defined value of 0.5, we believe that it is sufficiently small to account for the development of IH. When the flow rate is low, the TAWSS downstream of the toe may be <0.5 Pa. This phenomenon has been established for the ETS model; the second flow component and the size of the recirculation zone depend on the inlet angle[23,24] and the flow velocity. Our data suggest that ETS anastomoses are preferable because deSTS anastomoses are associated with low-WSS and high-OSI areas at the sidewall of the graft and its distal end.

Thrombosis is related to hemodynamic factors because blood flow transports cells and proteins to the thrombus and applies stresses that may disrupt it. Formation of a thrombus therefore depends on local flow conditions. The presence of a slow recirculation flow increases the near-wall residence time, resulting in platelet activation and fibrin thrombus formation, which in turn leads to the development of IH. In low-rate and low-shear recirculating flow, thrombi consist of red blood cells trapped in fibrin.[25] In this study, we identified slow recirculation zones in the proximal host artery and at the distal end. The flow rate in all phases was up to 0.08 m/s, being relatively slow (0.01 m/s or less) at the near end. Thrombosis could therefore form at the recirculation zones. However, a thrombosis changes the flow path and the hemodynamics, making it difficult to predict the final configuration.

In this study, we demonstrated that low-WSS and high-OSI areas extend distally and occur at the sidewall of the graft, its distal end, and just distal to the toe of the host artery. Given that a combination of low WSS and high OSI, or low WSS alone, favor the development of IH, our data suggest that ETS anastomoses are preferable.

However, hemodynamic variables are influenced by many factors, including anastomotic angle, caliber differences, compliance, and the inlet flow rate of the host artery. Li et al[7] have suggested that deSTS anastomoses may be a promising strategy for connecting small target coronary arteries; such anastomoses are commonly constructed. Further studies are needed to examine the hemodynamics in a deSTS model under various conditions and therefore enable selection of the optimal anastomosis technique according to the given conditions.

Study Limitations

Our main limitation is that we have used idealized geometries. Koyama et al[26] also examined bypass graft design based on the WSS-related parameters, an have already advocated the concept "basic idealized model" to lead generalized conclusions. They constructed a CFD model using patient data. However, our CFD model was confined to idealized models useful in elucidating geometrically driven homonymic differences between ETS and deSTS anastomoses and validating the findings. A patient-specific CFD model would provide better insights into the interaction between anastomotic geometries, hemodynamics and the pathogenesis of IH.

In this study, the discrepancies between simulation and experimental results may be attributable to background noise, wall reflection, the accuracy of the positioning of the measuring plane in PIV techniques, and the accuracy of the flowmeter. More importantly, discrepancies may be attrib-

utable to differences in the geometrical details of the resin and numerical models. In this study, we investigated a 10-times-actual-size model via PIV. Accurate measurement of WSS requires an analysis of detailed velocity profiles in an area near the wall, and this cannot be achieved with actual size models because they are too small. Our study design appears valid given that we found a fair match between the numerical and experimental data for the velocity vectors and the WSS distributions.

Conclusions

In this study, we comprehensively studied the hemodynamics of deSTS and ETS anastomosis models using both numerical simulations and PIV measurements. We found a fair match between the numerical and experimental data for the velocity profiles and WSS distributions under steady-flow conditions. In addition, the hemodynamic characteristics of the deSTS models are different from those of the ETS models in that there are recirculation zones, low and oscillating WSS areas at the distal end, just distal to the toe of the host artery, that may lead to IH formation. Further studies in which analyses are performed under various simulated conditions with actual models are needed.

Acknowledgments

This work was supported by The Japan Heart Foundation Research Grant from the Japan Heart Foundation.

Disclosure

The authors declare no conflicts of interest associated with this manuscript.

References

1. Bassiouny HS, White S, Glagov S, Choi E, Giddens DP, Zarins CK. Anastomotic intimal hyperplasia: Mechanical injury or flow induced. *J Vasc Surg* 1992; **15:** 708–717.
2. Sottiurai VS. Distal anastomotic intimal hyperplasia: Histocytomorphology, pathophysiology, etiology, and prevention. *Int J Angiol* 1999; **8:** 1–10.
3. Ghista DN, Kabinejadian F. Coronary artery bypass grafting hemodynamics and anastomosis design: A biomedical engineering review. *Biomed Eng Online* 2013; **12:** 129.
4. Owida, AA, Do H, Morsi YS. Numerical analysis of coronary artery bypass grafts: An over view. *Comput Methods Programs Biomed* 2012; **108:** 689–705.
5. Haruguchi H, Teraoka S. Intimal hyperplasia and hemodynamic factors in arterial bypass and arteriovenous grafts: A review. *J Artif Organs* 2003; **6:** 227–235.
6. Song MH, Tokuda Y, Ito T. Revival of the side-to-side approach for distal coronary anastomosis. *J Cardiothorac Surg* 2007; **2:** 2–7.
7. Li H, Xie B, Gu C, Gao M, Zhang F, Wang J, et al. Distal end side-to-side anastomoses of sequential vein graft to small target coronary arteries improve intraoperative graft flow. *BMC Cardiovasc Disord* 2014; **14:** 65.
8. Umezu M, Kawai J, Suehiro J, Arita M, Shiraishi Y, Iwasaki K, et al. Biomedical engineering analysis of effectiveness of cardiovascular surgery: Anastomosis methods for coronary artery bypass grafting. *Biocybern Biomed Eng* 2006; **26:** 61–67.
9. Galjee MA, van Rossum AC, Doesburg T, Hofman MB, Falke TH, Visser CA. Quantification of coronary artery bypass graft flow by magnetic resonance phase velocity mapping. *Magn Reson Imaging*1996; **14:** 485–493.
10. Ku DN, Giddens DP, Zarins CK, Glagov S. Pulsatile flow and atherosclerosis in the human carotid bifurcation. *Arteriosclerosis* 1985; **5:** 293–302.
11. Davies PF, Remuzzi A, Gordon EJ, Dewey CF, Gimbrone MA. Turbulent fluid shear stress induces vascular endothelial cell turnover in vitro. *Proc Natl Acad Sci U S A* 1986; **83:** 2114–2117.
12. Kamiya A, Bukhari R, Togawa T. Adaptive regulation of wall shear stress optimizing vascular tree function. *Bull Math Biol* 1984; **46:** 127–137.
13. Fry DL. Acute vascular endothelial changes associated with increased blood velocity gradients. *Circ Res* 1968; **22:** 165–197.
14. Sho E, Nanjo H, Sho M, Kobayashi M, Komatsu M, Kawamura K, et al. Arterial enlargement, tortuosity and intimal thickening in response to sequential exposure to high and low wall shear stress. *J Vasc Surg* 2004; **39:** 601–612.
15. Friedman M, Hutchins G, Bargeron C, Deters O, Mark F. Correlation between intimal thickness and fluid shear in human arteries. *Atherosclerosis* 1981; **39:** 425–436.
16. Moore Jr JE, Xu C, Glagov S, Zarins C, Ku D. Fluid wall shear stress measurements in a model of the human abdominal aorta: Oscillatory behavior and relationship to atherosclerosis. *Atherosclerosis* 1994; **110:** 225–240.
17. Casa LD, Deaton DH, Ku DN. Role of high shear rate in thrombosis. *J Vasc Surg* 2015; **61:** 1068–1080.
18. Longest PW, Kleinstreuer C, Deanda A. Numerical simulation of wall shear stress and particle-based hemodynamic parameters in pre-cuffed and streamlined end-to-side anastomoses. *Ann Biomed Eng* 2005; **33:** 1752–1766.
19. Niinami H, Takeuchi Y. Coronary artery bypass grafting using side-to-side anastomosis. *Kyobu Geka* 2000; **53:** 747–749.
20. Matsuyama K, Kuinose M, Koizumi N, Iwasaki T, Toguchi K, Ogino H. Coronary artery bypass grafting using side-to-side anastomosis with distal end clipping of the saphenous vein graft. *J Vasc Med Surg* 2014; **2:** 145, doi:10.4172/2329-6925.1000145.
21. Bonert M, Myers JG, Fremes S, Williams J, Ethier CR. A numerical study of blood flow in coronary artery bypass graft side-to-side anastomoses. *Ann Biomed Eng* 2002; **30:** 599–611.
22. Kabinejadian F, Chua LP, Ghista DN, Sankaranarayanan M, Tan YS. A novel coronary artery bypass graft design of sequential anastomoses. *Ann Biomed Eng* 2010; **38:** 3135–3150.
23. Pietrabissa R, Inzoli F, Fumero R. Simulation study of the fluid dynamics of aorto-coronary bypass. *J Biomech Eng* 1990; **12:** 419–424.
24. Hughes PE, How TV. Effects of geometry and flow division on flow structures in models of the distal end-to-side anastomosis. *J Biomech* 1996; **29:** 855–872.
25. Wootton DM, Ku DN. Fluid mechanics of vascular systems, diseases, and thrombosis. *Annu Rev Biomed Eng* 1999; **1:** 299–329.
26. Koyama S, Kitamura T, Itatani K, Yamamoto T, Miyazaki S, Oka N, et al. Impact of top end anastomosis design on patency and flow stability in coronary artery bypass grafting. *Heart Vessels* 2016; **31:** 643–648.

Supplementary Files

Supplementary File 1

Movie S1. Streamlines and vectors of a cross-section at the toe of the distal-end side-to-side (deSTS) model.

Supplementary File 2

Movie S2. Streamlines and vectors of a cross-section at the toe of the end-to-side (ETS) model.

Please find supplementary file(s);
http://dx.doi.org/10.1253/circj.CJ-17-0381